The role of chromium in iron-based high-temperature water-gas shift catalysts under industrial conditions

Ariëns, M. I.; Chlan, V.; Novák, P.; van de Water, L. G.A.; Dugulan, A. I.; Brück, E.; Hensen, E. J.M.

DOI
10.1016/j.apcatb.2021.120465

Publication date
2021

Document Version
Final published version

Published in
Applied Catalysis B: Environmental

Applied Catalysis B: Environmental 297 (2021) 120465

Contents lists available at ScienceDirect

Applied Catalysis B: Environmental

journal homepage: www.elsevier.com/locate/apcatb

The role of chromium in iron-based high-temperature water-gas shift catalysts under industrial conditions

M.I. Ariëns [a,b], V. Chlan [c], P. Novák [d], L.G.A. van de Water [e], A.I. Dugulan [a], E. Brück [a], E.J. M. Hensen [b,*]

[a] Fundamental Aspects of Materials and Energy, Delft University of Technology, Mekelweg 15, 2629 JB Delft, the Netherlands
[b] Laboratory of Inorganic Materials and Catalysis, Department of Chemical Engineering and Chemistry, Eindhoven University of Technology, P.O. Box 513, 5600 MB Eindhoven, the Netherlands
[c] Faculty of Mathematics and Physics, Charles University, V Holešovičkách 2, 180 00 Prague 8, Czech Republic
[d] Institute of Physics of ASCR, Cukrovarnická 10, 162 53 Prague 6, Czech Republic
[e] Johnson Matthey, PO Box 1, Belasis Avenue, Billingham, Cleveland, TS23 1LB, United Kingdom

ARTICLE INFO

Keywords:
Water-gas shift reaction
Iron oxide
Chromium
Promotion
Mössbauer spectroscopy

ABSTRACT

Chromium promotion of iron oxide based water-gas shift (WGS) catalysts prepared *via* co-precipitation/calcination was investigated. Mössbauer spectroscopy and XRD evidence that chromium is incorporated in the calcined hematite (α-Fe_2O_3) precursor irrespective of the doping level (0–12 wt.%). CO-TPR shows chromium delays the reduction of hematite and the active magnetite (Fe_3O_4) phase. WGS activity was evaluated under realistic conditions for 4 days. Enhanced CO conversion was observed with increased chromium doping. Mössbauer spectra indicate that chromium incorporates into octahedral sites of magnetite and prevents reduction of Fe^{3+} to Fe^{2+} during formation of the active phase, leading to an increased Fe^{3+}/Fe^{2+} ratio in octahedral sites. The higher Fe^{3+}/Fe^{2+} ratio did not affect the high CO conversion associated with the structural stabilization mechanism of Cr-doping. Interpretation of the Mössbauer spectra was supported by computational modelling of various chromium and vacancy-doped magnetite structures. The bulk structure of an *in situ* prepared chromium-doped high-temperature WGS catalyst is best described as a partially oxidized chromium-doped magnetite phase. No surface effects of Cr-doping were found.

1. Introduction

Hydrogen is an important reagent used mainly in industrial ammonia synthesis [1,2]. Traditionally, hydrogen is produced by the steam methane reforming (SMR) process, which involves the water-gas shift (WGS) reaction to maximise hydrogen production (1) [1,3]. As the WGS reaction is mildly exothermic ($\Delta H = -40.6$ kJ/mol), high CO conversion is favoured at low temperature [1]. In practice, the WGS section is divided into two steps: (i) a high-temperature shift (HTS) step, which is typically performed at 350–450 °C over an iron-chromium-copper-oxide catalyst and removes the bulk of CO from the synthesis gas product stream from the SMR step, and (ii) a low-temperature shift (LTS) step, performed at temperatures in the range of 190–250 °C on a more active copper-zinc-alumina catalyst [3–6]. In the HTS step, the CO concentration is typically decreased from 10–15% CO to 2–4 % CO [4].

$$H_2O + CO \rightleftarrows CO_2 + H_2 \quad (1)$$

The active phase of HTS catalysts, magnetite, is formed *in situ* by partial reduction of hematite or other bulk Fe^{3+}-oxide precursors such as maghemite (γ-Fe_2O_3) [5,7]. Magnetite has an inverse spinel structure with the formula AB_2O_4 [7]. In stoichiometric magnetite the tetrahedral A-sites are occupied by Fe^{3+} and the octahedral B-sites by an equimolar mixture of Fe^{2+} and Fe^{3+} [8]. The activity of iron-based WGS catalysts is often linked to the Fe^{2+}/Fe^{3+} redox couple in the octahedral sites [1,9]. Boreskov et al. [10] showed that Fe^{2+} can be oxidised by H_2O to Fe^{3+} and Fe^{3+} can be reduced to Fe^{2+} by CO. More recently, Keturakis et al. [5] confirmed that the HTS reaction follows a redox mechanism and that oxygen atoms at the surface are the most abundant reactive intermediates. Magnetite as such is prone to thermal agglomeration and over-reduction under practical WGS conditions [1,2]. The addition of chromium to the Fe^{3+}-oxide precursor typically increases the stability of

* Corresponding author.
E-mail address: e.j.m.hensen@tue.nl (E.J.M. Hensen).

https://doi.org/10.1016/j.apcatb.2021.120465
Received 20 April 2021; Received in revised form 10 June 2021; Accepted 15 June 2021
Available online 25 June 2021

magnetite towards sintering and reduction of the active phase to Wüstite (FeO), metallic iron, and iron carbides. Metallic iron and iron carbides are highly undesired, because they catalyse methanation and Fischer-Tropsch side-reactions. Keturakis et al. [5] recently showed that hexavalent chromium, which is present on the surface of freshly calcined catalysts, is reduced to Cr^{3+} upon exposure to WGS feed mixtures. According to Keturakis et al., the main role of chromium is that of a structural promoter, decreasing sintering and over-reduction. Khan and Smirniotis [7] showed that hematite is converted into magnetite under atmospheric pressure HTS conditions and that chromium stabilizes the active phase against sintering. The positive effect of chromium against sintering of the active phase was later confirmed by Reddy et al. [11] Another proposed role of chromium is that of a chemical promoter, enhancing the WGS activity of magnetite by involvement of the Cr^{6+}/Cr^{3+} redox couple [2,12]. This view is not supported by more recent findings however [13]. Robbins et al. [14] and Topsøe and Boudart [15] showed by Mössbauer spectroscopy that chromium is incorporated in octahedral sites of magnetite. Reddy et al. [16] recently confirmed this for their WGS catalysts. The exact position of chromium in the octahedral sites is however still unknown. Robbins et al. [14] reported that chromium replaces an equal amount of Fe^{2+} and Fe^{3+} in the octahedral sites, while Topsøe and Boudart [15] could not confirm this for their WGS catalysts. A difference between these studies is that only the work of Topsøe and Boudart involved Mössbauer spectroscopy characterization of samples after exposure to WGS reaction conditions. A literature review by Zhu and Wachs [1] mentioned that Cr^{3+} replaces Fe^{3+} at octahedral sites of magnetite, which is the active phase for the HTS reaction. Nevertheless, these authors recently referred to the Robbins model as the correct model of chromium incorporation [13]. Rangel et al. [17] showed that chromium-doped magnetite, prepared by heating chromium-containing iron(III)hydroxyacetates, resulted in a lower Fe^{2+}/Fe^{3+} ratio compared to stoichiometric magnetite. This was explained by the preference of Cr^{3+} to occupy octahedral sites, which prevents Fe^{2+} formation. More Fe^{2+} was observed upon use of their catalysts in the WGS reaction. Commercial HTS catalysts also contain small amounts of CuO to enhance CO conversion [18]. Copper is known to form a separate metallic phase, which may be partially covered by an iron oxide over-layer during HTS conditions. These partially covered Cu° nanoparticles enhance CO conversion by providing additional active sites [19,20].

Concerns about the presence of Cr^{6+} in the fresh catalyst [21] have resulted in the search for novel compositions in which chromium is replaced by other dopants [6,13]. Rational design of such a catalyst is hindered by a lack of clear understanding of the working mechanism of Cr stabilization and the local structure of Cr in magnetite. The recent insights discussed above for chromium-doped iron oxide catalysts were mostly obtained under conditions different from industrial HTS conditions, *i.e.*, atmospheric pressure and/or non-representative WGS reaction feed mixtures. A thorough characterization study of such catalysts aged for a prolonged time under industrially relevant HTS conditions is still lacking.

The aim of this study is to understand better the role of chromium in Fe-based HTS catalysts with a focus on the location of chromium in the active magnetite phase obtained when the catalyst precursor is exposed to industrially relevant WGS conditions [4]. A range of Fe-Cr mixed oxide catalysts were prepared *via* a single step co-precipitation/calcination route. Dedicated ageing protocols were used including prolonged exposure to HTS conditions, industrially relevant gas feed compositions, and high pressure. Catalysts were aged at 2 and 25 bar to investigate the influence of the reaction pressure.

The bulk and surface properties of the aged catalysts were investigated by XRD, XPS and Mössbauer spectroscopy. XRD, Mössbauer spectroscopy, CO-TPR, N_2-physisorption, and TEM were also applied to gain insight into the chromium in the catalyst precursors. Mössbauer spectroscopy is a highly sensitive bulk technique based on the effect discovered by Mössbauer in 1958, involving the nearly recoil-free emission and absorption of nuclear X-rays in solids [22]. This technique is extremely useful for the study of iron catalysts [23,24]. Its sensitivity for iron allows for deconvolution of Mössbauer spectra of the active magnetite phase into separate sub-spectra for the tetrahedral and octahedral Fe sites from which detailed information on local dopant incorporation and oxidation state can be obtained. The interpretation of experimental Mössbauer parameters for chromium-doped magnetite catalysts was supported by computing hyperfine parameters of a range of magnetite structures containing iron vacancies or chromium in octahedral sites. Chromium-doping in tetrahedral positions was not considered based on existing experimental evidence [14,15,17]. The formal composition of magnetite is $[Fe^{3+}]_A[Fe^{2+}Fe^{3+}]_B[O^{2-}]_4$ where cations in A and B sites are tetrahedrally and octahedrally coordinated by oxygen, respectively [8,25]. The B sublattice exhibits mixed-valance character. The structure of magnetite depends on the temperature: the inverse cubic spinel of magnetite above the Verwey phase transition at 120 K, characterized by equivalency of all A and B sites, transforms in the monoclinic *Cc* structure with 8 different groups of crystallographically equivalent A sites and 16 different groups of crystallographically B sites.

2. Experimental

2.1. Catalyst preparation

Catalysts were prepared by a single-step co-precipitation/calcination method described elsewhere [26]. Briefly, appropriate amounts of chromium and iron nitrates were dissolved in deionised water and precipitated by addition of an aqueous NaOH solution. The resulting slurry was aged at 60 °C and pH 10 for 1 h, after which it was filtered and washed before drying at 150 °C for 3 h and calcination at 400 °C for 4 h in air. A total of 5 catalysts with compositions of *x* wt.% Cr_2O_3 ($x = 0$, 1, 4, 8, and 12) in α-Fe_2O_3 were prepared in this way. Catalysts were denoted as Cr(*x*) in the following.

2.2. Catalyst characterization

X-ray powder diffraction (XRD) patterns were recorded on a PANalitical X'pert pro diffractometer between $10^{\circ} < 2\theta < 100^{\circ}$, step size 0.008°, using Cu-K_α radiation. The HighScore Plus software was used for spectral fitting. Approximately 30 mg of sample was placed in an airtight sample holder and characterised at room temperature. The aged catalysts were stored and measured under Ar, calcined catalysts were stored and measured in air.

Temperature programmed reduction (CO-TPR) experiments were performed in a quartz tube suspended in a tubular oven. In a typical experiment, 50 mg freshly calcined catalyst was diluted with 200 mg SiC and placed in between quartz wool plugs in a quartz reactor tube. The samples were pre-treated at 400 °C under 10 % O_2/He flow (50 mL min^{-1}) for 1 h. The reactor was then purged with He and cooled to room-temperature. The temperature was subsequently ramped to 650 °C under a constant flow of 10 % CO/He (50 mL min^{-1}). A heating rate of 5 °C min^{-1} was maintained during pre-treatment and the TPR experiment. Product formation was monitored by an online mass spectrometer (ESS, GeneSys Evolution), different reduction temperatures were determined by the shift in CO_2 evolution peak. A Mössbuaer spectrum was recorded of a Cr(0) sample after stopping the reaction at 411 °C by replacing the CO/He feed with He followed by cooling to room temperature. The sample was then exposed to air and a Mössbauer spectrum was recorded at room temperature.

Transmission **^{57}Fe Mössbauer spectra** were recorded in constant-acceleration and sinusoidal velocity spectrometers [27] using a ^{57}Co (Rh) source. Samples (~30 mg) were mixed with graphite and placed between Kapton foil in a copper ring. In the room-temperature Mössbauer measurements, the source and absorber were kept at ambient conditions, while in the low-temperature measurements the

Table 1
Fe-oxide reference structures used to determine hyperfine parameters of Fe nuclei using DFT.

Structure[a]	Name[b]	Cr content (%)	Content of Fe vacancies (%)	Space group	Lattice parameters (Å)
Fe_3O_4	Fe_3O_4 (magnetite)	0	–	Fd-3m	a = 8.424
$(Fe_8)[CrFe_{15}]O_{32}$	Cr-1	4.2	–	R-3m	a = 11.901 c = 14.574 γ = 120°
$(Fe_8)[Cr_2Fe_{14}]O_{32}$	Cr-2 (I)	8.3	–	C2	a = 11.932 b = 25.377 c = 11.853 γ = 160.6°
	Cr-2 (II)			Cm	a = 11.933
	Cr-2 (III)			C2/m	b = 8.410 c = 11.854 γ = 89.5°
$(Fe_2)[CrFe_3]O_8$	Cr-4	16.7	–	R-3m	a = 5.870 c = 14.883 γ = 120°
$(Fe_2)[Cr_2Fe_2]O_8$	Cr-8	33.3	–	Fm-3	a = 8.395
$(Fe_{16})[\square Fe_{31}]O_{64}$	Vac-0.5	–	2.1	R-3m	a = 11.914 c = 29.183 γ = 120°
$(Fe_{24})[\square_8Fe_{40}]O_{96}$	Vac-8/3 (maghemite)	–	11.1	$P4_12_12$	a = 8.503 c = 25.456
$(Fe_2)[\square Fe_3]O_8$	Vac-4	–	16.7	R-3m	a = 5.876 c = 14.394 γ = 120°

[a] Fe ions in tetrahedral positions are shown in parentheses (), Fe ions in octahedral position in brackets []. Octahedral metal vacancies are indicated by a square □.
[b] Cr-*x* refers to chromium-doped models with *x* indicating the number of octahedral Fe ions being replaced by Cr^{3+} per unit cell. Vac-*x* refers to structures containing octahedral vacancies with *x* referring the number of such vacancies per unit cell.

source and absorber were cooled in liquid He. The temperature was constant during the measurements. Mössbauer spectra were recorded in a standard He bath cryostat. The source if connected *via* a rod to the transducer and the direction of the γ-beam is vertical. The absorber and source can be moved independently from the cryostat which allows for the recording of room-temperature spectra outside of the cryostat without the need for heating the cryostat to room-temperature. Velocities are reported relative to α-Fe at room-temperature. The Mosswinn 4.0 software was used for spectral fitting [28]. Samples were stored under argon atmosphere prior to and during characterisation.

N_2 physisorption experiments were performed on a Micromeritics 2420 ASAP instrument. Samples were degassed with nitrogen at 140 °C for at least 1 h prior to characterisation. A p/p_0 range of 0.005 to 0.995 was used for the absorption/desorption measurements. Around 500 mg sample was used for each measurement.

Transmission electron microscopy (TEM) images were recorded on a FEI Tecnai 20 (type Sphera) TEM. Samples were suspended in ~3 mL acetone, sonicated for ~30 min in a sonication bath, and subsequently dispersed over a Cu grid containing holey carbon film. Particle size averages were obtained by counting 200 particles per sample using ImageJ software.

X-ray photoelectron spectra (XPS) were recorded on a Thermo Scientific K-Alpha spectrometer using an aluminium anode (Al Kα =1486.6 eV). Binding energy calibration was performed relative to adventitious carbon at BE =285 eV. The CasaXPS software (version 2.3.19PR1.0) was used for spectral fitting. Samples were transferred to the spectrometer under vacuum. The pressure in the XPS analysis chamber was typically below 10^{-9} mbar, while the pressure during sample transfer was in the range of 0.1 mbar.

Catalytic activity measurements were performed in a custom-built set-up comprising 6 parallel fixed-bed microreactors with an inner diameter of 3 mm and a length of ~20 cm, operated under identical conditions (temperature, pressure, inlet gas composition) at 2 or 25 bar. Thermocouples placed in the jacket walls of the microreactors, 10 cm below the reactor inlet, ensured isothermal operation. The microreactors were housed in a nitrogen-purged oven. Liquid water was added using peristaltic pumps and vaporised inside the oven prior to mixing with the dry gas feed. Exit gas compositions were measured at 1 bar using an online infrared gas analyser (Emerson X-Stream 2), capable of simultaneous analysis of CO, CO_2 and methane. The relative error in the gas analysis values was estimated to be ~5%. The exit gas compositions of the different reactors were collected after a stabilisation period of 45 min per reactor, after which time the next reactor stream was selected by means of an automated Valco selection valve. In a typical experiment, the reactor tubes were charged with 100 mg catalyst diluted with 500 mg α-Al_2O_3. The reactors were purged with nitrogen after which the temperature was raised to 250 °C at a rate of 2 °C min^{-1}. Steam was added followed by the addition of reaction gas to reach the desired composition (37 % H_2, 9% CO, 4% CO_2, 17 % N_2, 33 % H_2O) representative for industrial HTS conditions. The temperature was subsequently ramped to 450 °C at a rate of 1 °C min^{-1} and maintained for 24 h to age the catalyst at equilibrium conversion, while CO conversion was recorded. The temperature was then lowered to 360 °C and the activity was measured for 24 h at conditions relatively far away from thermodynamic equilibrium. A second thermal ageing step was carried out at 450 °C for 24 h followed by additional activity measurement at 360 °C for 24 h. The temperature was then lowered to 250 °C and the H_2, CO, and CO_2 flows were switched to N_2. When no more CO was observed in the effluent stream, steam addition was stopped and the catalysts were cooled to room-temperature in nitrogen flow. The reactors were then closed off and transferred to a glovebox where the catalysts were removed under inert atmosphere to ensure no air exposure occurred. The catalysts were finally stored under an argon atmosphere prior to characterization.

2.3. Computational modelling

Hyperfine parameters required for simulating Mössbauer spectra were calculated based on spin-polarized density functional theory (DFT) using WIEN2k [29], which employs full-potential augmented plane-wave method to describe the ion-electron interactions. The size of the basis set and the number of *k*-points in reciprocal space were carefully converged. Electron-exchange correlation was represented by the generalized gradient approximation (GGA) with the Perdew-Burke-Ernzerhof (PBE) exchange-correlation functional. Radii of the atomic spheres for Fe, Cr, and O atoms were chosen as 2.0, 1.85,

Table 2
Selected physico-chemical properties of the calcined catalysts.

Sample	d (nm)		BET SA ($m^2\ g^{-1}$)	V_{tot} ($cm^3\ g^{-1}$)	Average d_{pore} (nm)	Cr_2O_3[b] (wt. %)	Na_2O[b] (wt. %)
	TEM	XRD[a]					
Cr(0)	28 ± 17	44	45	0.22	19.9	0.0	0.6
Cr(1)	18 ± 11	38	56	0.22	15.7	0.8	0.6
Cr(4)	17 ± 7	29	81	0.23	11.2	3.9	0.7
Cr(8)	12 ± 4	25	110	0.25	9.2	7.3	1.6
Cr(12)	12 ± 4	24	125	0.31	9.9	11.3	2.1

[a]Calculated from XRD line broadening analysis using the Scherrer equation.
[b]Obtained by XRF analysis. The Cr_2O_3 content is slightly lower than intended, possibly due to the presence of some residual Na_2O [33].
[c]Surface area (SA) determined by the Brunauer-Emmett-Teller (BET) method, pore volume (V_{tot}), and pore diameter (d_{pore}) using the BJH (Barrett-Joyner-Halenda) method.

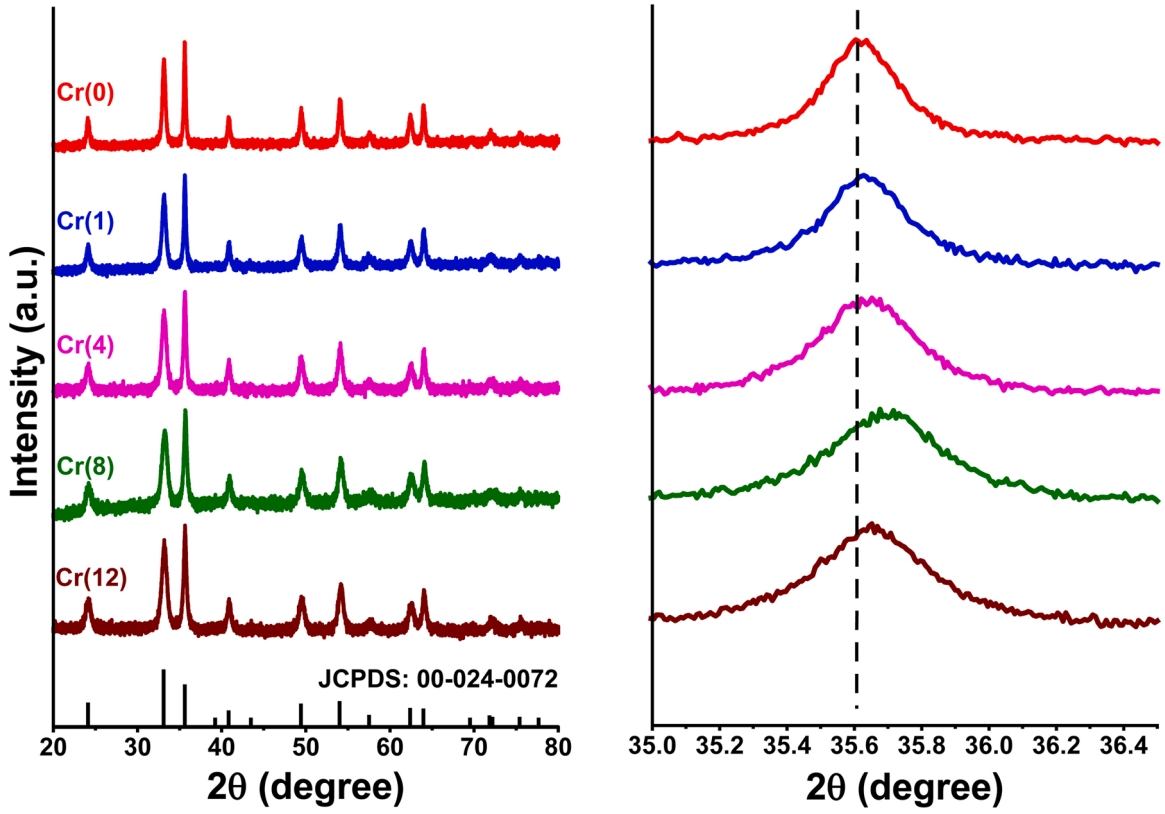

Fig. 1. XRD patterns of freshly calcined catalysts (right panel shows magnified region around the (110) reflection of hematite).

and 1.5 bohr units (1 bohr unit, $a_0 = 5.29 \times 10^{-11}$ m).

The isomer shift (IS) in Mössbauer spectra scales linearly with the electron charge density at the Fe nucleus relative to a reference, which is typically metallic bcc α-Fe. The charge density at a particular Fe site was determined by DFT as the charge within a uniformly charged Thomson sphere with radius $R_0 = 5{\times}10^{-5}\ a_0$. The computed charge difference $\Delta\rho$ with the reference obtained in this way was converted to the IS using $IS = \alpha * \Delta\rho$, where α was obtained by calibration using a set of 11 experimental IS values of Fe reference compounds [30]. The original set of 11 compounds was extended to 16 reference materials in this work, yielding $\alpha = -0.32 \pm 0.02$ mm $s^{-1}\ e^{-1}\ a_0^3$.

The total local magnetic field at Fe nucleus was calculated by DFT as a sum of all relevant contributions. The hyperfine fields induced by electron orbital moment and due to interaction with the electron spin (within the dipole limit) were obtained straightforwardly from the occupation matrices of the Fe 3d electrons. To compute the contact part of the hyperfine field, the method of Novák and Chlan was used [31], involving calculation of the spin magnetic moments of the Fe 3d and 4 s electrons. Additionally, the dipolar field from the neighbouring atomic moments in the lattice was evaluated by direct summation of moments within a sufficiently large Lorentz sphere (radius = 250 a_0).

Various structural models of magnetite were employed to determine the total hyperfine magnetic field and the isomer shift at the Fe nuclei including magnetite, octahedral-vacancy-containing magnetite ($Fe_{3(1-\delta)}O_4$), and chromium-doped magnetite ($Fe_{3-x}Cr_xO_4$) where Fe in octahedral positions was replaced by Cr. The structures, their space groups and optimized lattice parameters are listed in Table 1. All structural models were considered within one conventional spinel unit cell (or its equivalent for cases with different symmetry). For the lowest Cr concentrations the number of possible models is reasonable (one for 4 % Cr and three for 8 % Cr), however, for larger Cr concentrations the number of variants would be unfeasible, and thus only the most symmetric models were selected. In addition to investigating the impact of chromium content, the three different Cr-2 models allow to estimate the impact of Cr arrangement on the observed quantities. The Cr arrangement in all these DFT model structures is fixed and repeated infinitely by periodic boundary conditions and, therefore, cannot represent the complete structural variation of the experimental sample. Hence, we

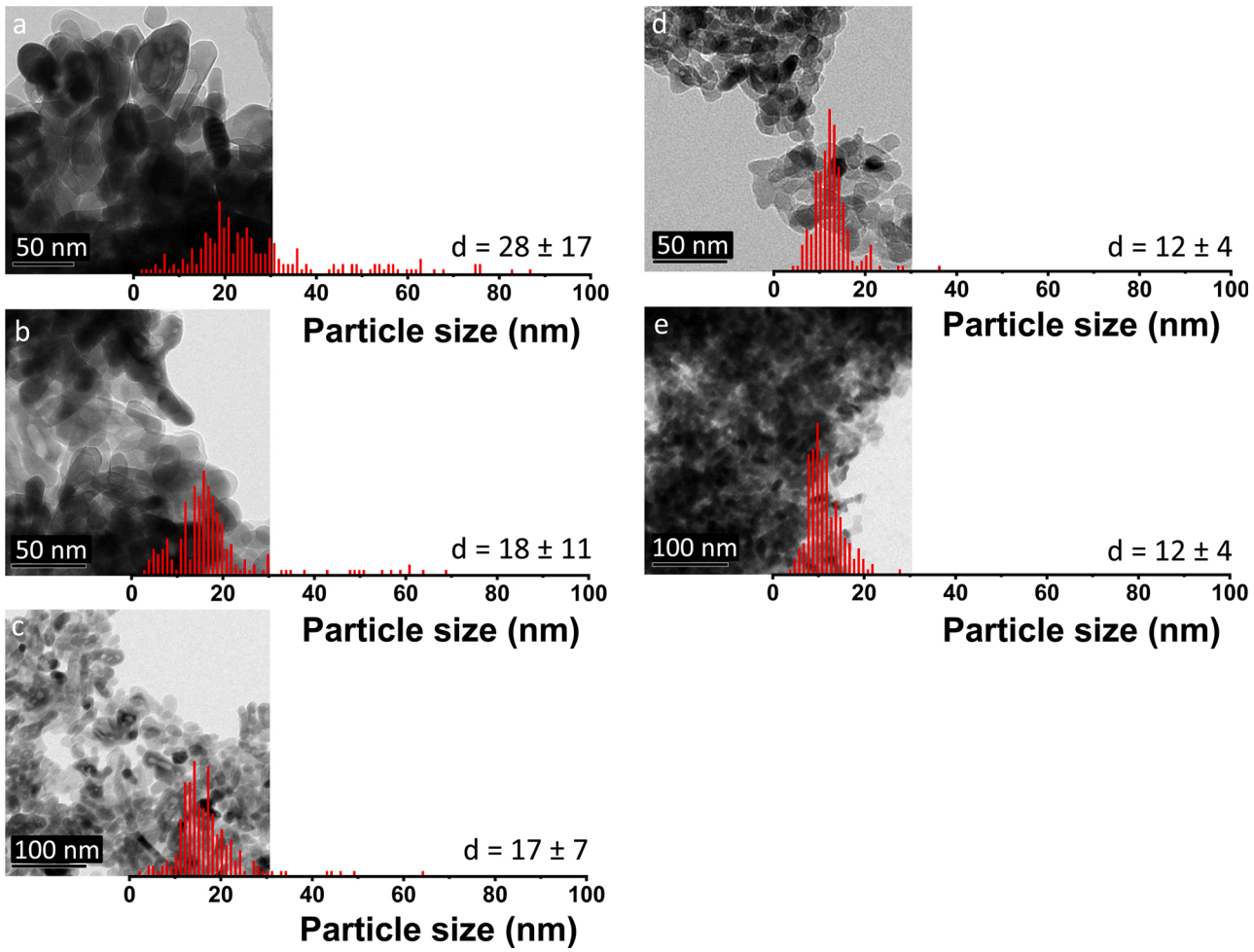

Fig. 2. Particle sizes of calcined catalysts as determined by TEM analysis: (a) Cr(0), (b) Cr(1); (c) Cr(4); (d) Cr(8), and (e) Cr(12).

used parameters that were the weighted averages within each Fe sublattice (A or B sites in the AB_2O_4 structure of magnetite).

3. Results and discussion

3.1. Calcined catalysts

Chromium-doped iron oxide catalysts were prepared using a co-precipitation/calcination method adapted from Meshkani and Rezaei [26]. Routine physico-chemical properties of the calcined catalysts are shown in Table 2. XRD patterns of freshly calcined catalysts are presented in Fig. 1. The main reflections in the XRD patterns belong to hematite, irrespective of chromium doping level. The position of the (110) reflection of hematite shifts to higher 2θ values in the chromium doped samples compared to the non-doped Cr(0). The shift of the hematite diffraction lines to higher 2θ values points to contraction of the unit cell, which can be explained by the incorporation of chromium cations (Cr^{3+}) with a smaller radius (62 pm) than iron cations (Fe^{3+}, 65 pm) in the host structure. No apparent trend in 2θ values upon increased chromium doping was observed however, possibly due to the similar ionic radii of Cr^{3+} and Fe^{3+} ions causing only small shifts. No other phases were observed, indicating that pure hematite was formed. This, however, does not exclude the presence of small (< 3 nm) or amorphous oxides of iron or chromium [32].

XRD line broadening analysis shows a decreasing crystallite size with increased chromium content from 44 nm for Cr(0) to 25 nm for Cr(8) (Table 2). The average crystallite sizes of the Cr(8) and Cr(12) samples were similar. Average particle sizes obtained by TEM analysis (Fig. 2) show a similar trend. The average particle size decreased from 28 ± 17 nm for Cr(0) to 12 ± 4 nm for Cr(8). The average particle size of the Cr(8) and Cr(12) sample as judged from TEM analysis were again similar. The trends in particle size established by TEM and XRD analysis are confirmed by the surface areas determined by N_2 physisorption (Table 2), showing a higher surface area with increasing chromium content.

Room-temperature Mössbauer spectra are shown in Fig. 3. These spectra contain a magnetically split sextet with isomer shift (IS) values of ~0.38 mm s^{-1} and quadrupole splitting (QS) values of ~-0.22 mm s^{-1}, irrespective of the chromium content (Table 3). These parameters, in combination with an average hyperfine magnetic field between 50.5 T and 47.3 T, confirm that the sample consists of hematite [34,35], in agreement with the XRD analysis. The hyperfine magnetic field distribution as displayed in Fig. 4 becomes broader with increasing chromium content. Such broadening can arise from a decrease in hematite particle size and/or the incorporation of a dopant in hematite [36]. We already discussed that the average particle size of the hematite phase decreased with increasing chromium content (Table 2). Therefore, we cannot unequivocally assign the broadening in the hyperfine magnetic field distribution to increasing levels of chromium doping. The similar particle sizes determined for the Cr(8) and Cr(12) samples provide a strong indication that the broadening of the hyperfine magnetic field distribution with increasing chromium content from Cr(8) to Cr(12) is the result of the incorporation of additional chromium into hematite. The superparamagnetic (SPM) phase with an isomer shift of 0.38 mm s^{-1} (Table 3), which is observed in the Mössbauer spectrum of the Cr(12) sample, points to a fraction of small particles of an Fe-oxide phase with

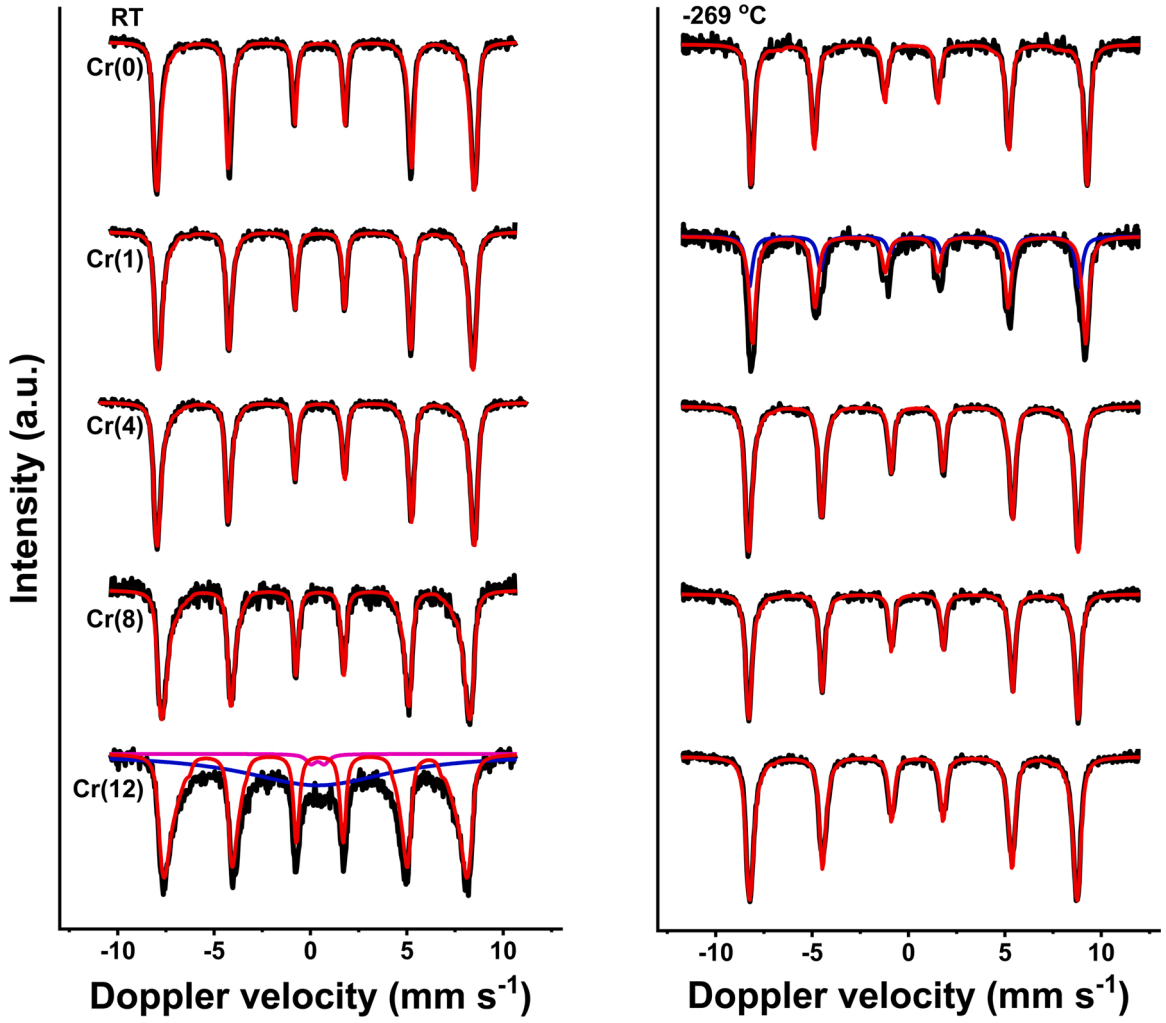

Fig. 3. Mössbauer spectra calcined of catalysts recorded at room-temperature (left) and −269 °C (right).

Table 3
Mössbauer parameters of freshly calcined samples obtained at room-temperature (RT) and −269 °C.

Measurement Temperature	Sample	IS (mm s^{-1})	QS (mm s^{-1})	Hyperfine field (T)	Γ (mm s^{-1})	Phase	Spectral contribution (%)
RT	Cr(0)	0.38	−0.23	50.5†	0.23	α-Fe_2O_3	100
	Cr(1)	0.38	−0.21	50.1†	0.23	α-Fe_2O_3	100
	Cr(4)	0.38	−0.22	50.5†	0.24	α-Fe_2O_3	100
	Cr(8)	0.38	−0.21	48.5†	0.25	α-Fe_2O_3	100
	Cr(12)	0.37	−0.22	47.3†	0.32	α-Fe_2O_3	54
		0.38*	0.69	–	0.60	Fe^{3+} SPM	2
		0.38*	–	–	9.28	Fe^{3+} SPM	44
−269 °C	Cr(0)	0.35	0.40	53.6†	0.28	α-Fe_2O_3 AF[c]	100
	Cr(1)	0.36	0.39	53.7†	0.40	α-Fe_2O_3 AF	68
		0.35	−0.10	53.2†	0.40	α-Fe_2O_3 WF[c]	32
	Cr(4)	0.35	−0.19	52.8†	0.30	α-Fe_2O_3	100
	Cr(8)	0.36	−0.21	52.7†	0.26	α-Fe_2O_3	100
	Cr(12)	0.36	−0.20	52.4†	0.33	α-Fe_2O_3	100

[a]Fixed values are marked with an asterisk (*), average values with a dagger (†).
[b]Experimental uncertainties: Isomer shift: IS ± 0.01 mm s^{-1}, quadrupole splitting: QS ± 0.01 mm s^{-1}, line width: Γ ± 0.01 mm s^{-1}, hyperfine magnetic field: ± 0.1 T, spectral contribution: ± 3%.
[c]AF (antiferromagnetic), WF (weakly ferromagnetic) [35].

high-spin Fe^{3+} ions in octahedral positions [24]. Based on the Mössbauer parameters of the SPM phase alone, it cannot be established what bulk Fe^{3+}-oxide phase is present.

To investigate the SPM fraction observed for Cr(12) in the room-temperature Mössbauer spectrum in more detail, a Mössbauer spectrum was recorded at −269 °C to regain magnetic splitting. The low-temperature Mössbauer spectra (Fig. 3) and the deconvolution results (Table 3) confirm the presence of a single hematite phase in Cr(12), indicating that the SPM fraction observed in the room-temperature Mössbauer spectra is hematite. In the Mössbauer spectrum of Cr(0) measured at −269 °C, a hyperfine magnetic field of 53.6 T was observed with a QS value of 0.40 mm s^{-1} (Table 3). The higher hyperfine

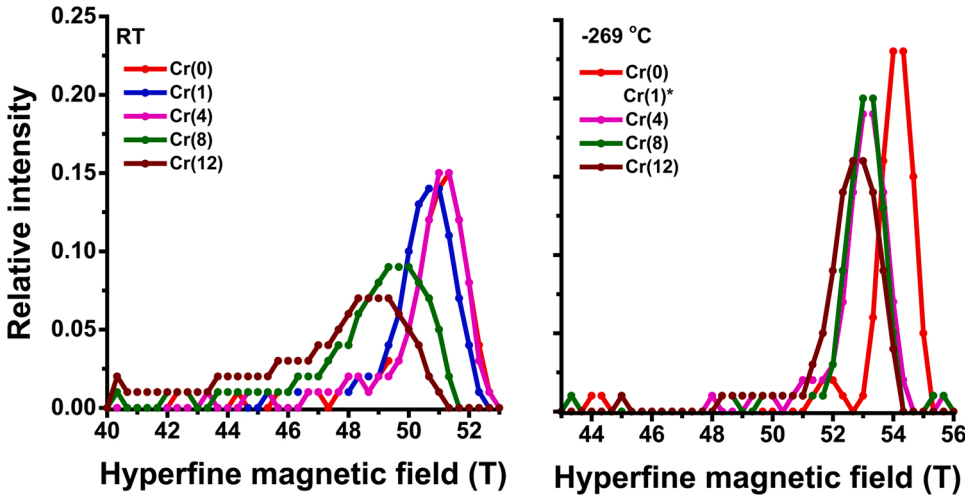

Fig. 4. Hyperfine magnetic field distributions obtained by fitting of the Mössbauer spectra recorded at room-temperature (left) and −269 °C (right) (* No hyperfine magnetic field distribution was fitted for the spectrum Cr(1) recorded at −269 °C because of a partial Morin transition, *cf.* Fig. 3, Table 3).

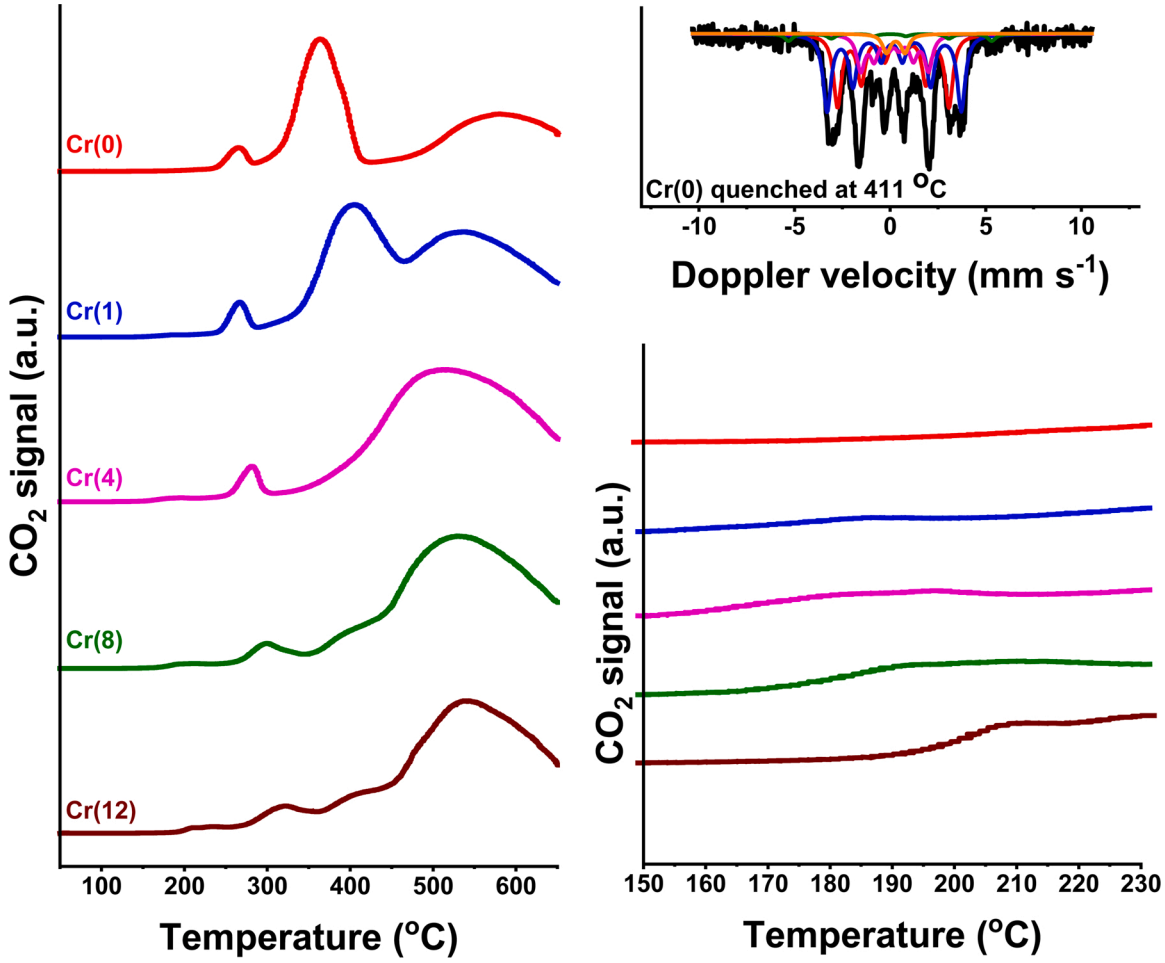

Fig. 5. CO-TPR patterns from 50 °C to 650 °C (left) and from 150 °C to 230 °C (right) of calcined catalysts. Mössbauer spectrum recorded after quenching Cr(0) at 411 °C. Sub-spectra of χ-Fe_5C_2(I), χ-Fe_5C_2(II), and χ-Fe_5C_2(III) are indicated in red, blue, and magenta, respectively. The sub-spectrum of α-Fe is shown in green, SPM Fe_xC in orange.

magnetic field of Cr(0) compared to the Cr(4)-Cr(12) samples (~52.7 T) and the QS value of ~0.40 mm s^{-1} indicate that hematite underwent the Morin transition [37]. The Morin transition occurs for hematite particles larger than 20 nm [35]. This transition is observed for Cr(0), which is the only sample containing hematite particles larger than 20 nm (Table 2). In the Cr(1) sample, two spectral contributions of hematite can be distinguished (Fig. 3). For the antiferromagnetic phase, the occurrence of the Morin transition indicates that this sample contains a

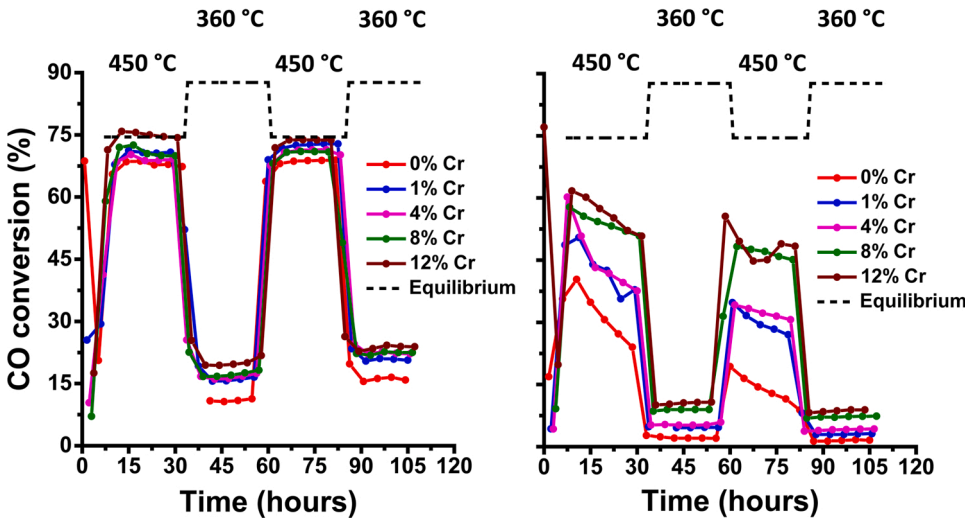

Fig. 6. CO conversion with time on stream during HTS at (left) 25 bar and (right) 2 bar (37 % H_2, 9% CO, 4% CO_2, 17 % N_2, 33 % H_2O, 360-450 °C). Methane formation was monitored throughout the catalytic tests and did not exceed 0.16 % (25 bar) and 0.06 % (2 bar) of the exit stream.

fraction of particles with a size larger than 20 nm. The Mössbauer spectra of Cr(4), Cr(8), and Cr(12) show a single sextet belonging to hematite (Fig. 3, Table 3). As mentioned above, the broadening of the hyperfine magnetic field distribution from Cr(8) to Cr(12) points to chromium incorporation into hematite. Thus, the low-temperature Mössbauer measurements provide strong evidence that the superparamagnetic Fe^{3+}-oxide phase observed in the Cr(12) sample at room temperature belongs to chromium-doped hematite.

The influence of chromium on the reducibility of the calcined catalysts was determined by CO-TPR (Fig. 5). The TPR patterns consist of two main reduction peaks, representing the reduction of hematite to magnetite (Fe_3O_4), and the further reduction of magnetite to metallic Fe, possibly followed by carburization. A Mössbauer spectrum recorded after quenching a TPR experiment of Cr(0) at 411 °C (Fig. 5) revealed the nearly complete transformation to Hägg-carbide (χ-Fe_5C_2) with only a small amount of α-Fe (3.6 %) remaining. This shows that the

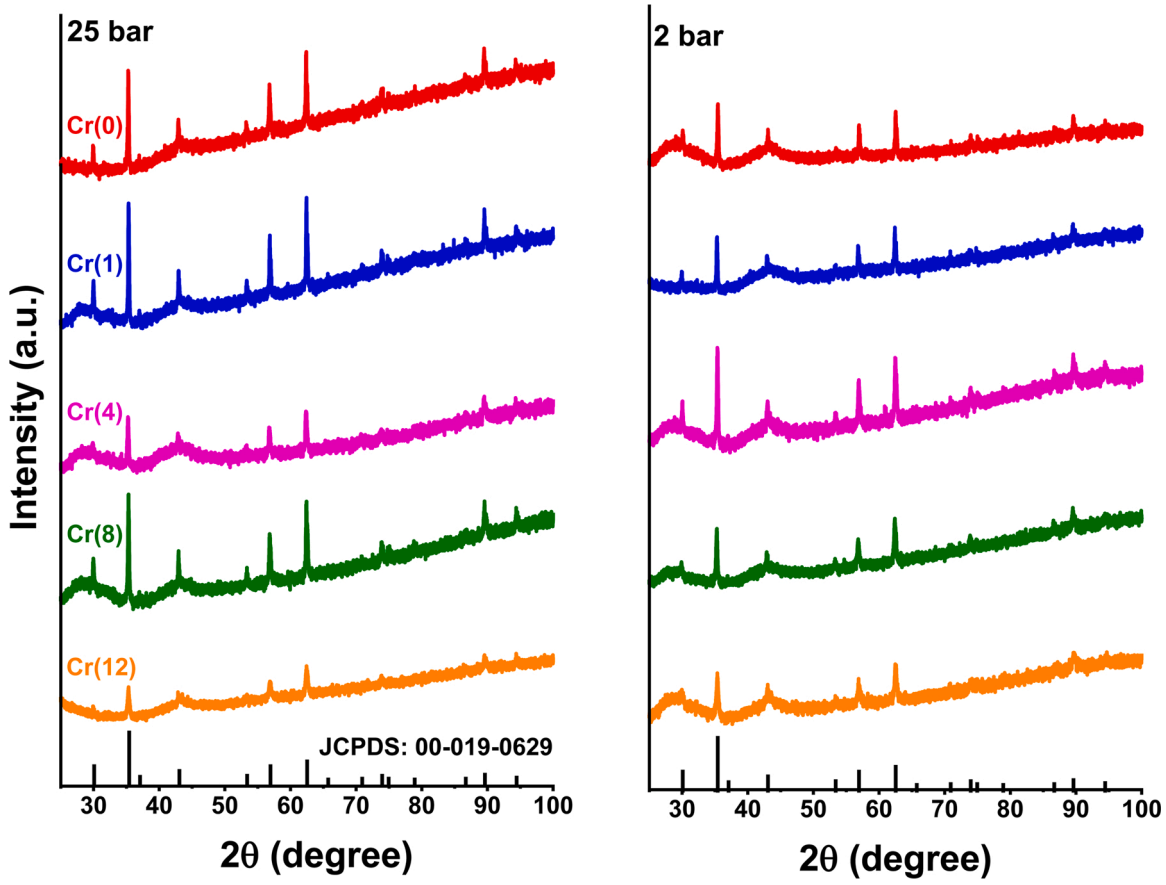

Fig. 7. XRD patterns of discharged catalysts after treatment under HTS conditions for 4 days at 25 bar (left) and 2 bar (right). Magnetite reference: JCPDS no. 00-019-0629.

Table 4
Average crystallite size of calcined hematite in fresh and activated magnetite phase in used catalysts.

Sample	dXRD (nm)[a]		
	Calcined	25 bar	2 bar
Cr(0)	44	74	71
Cr(1)	38	89	85
Cr(4)	29	55	52
Cr(8)	25	64	41
Cr(12)	24	30	27

[a] Determined using the Scherrer equation.

chromium-free hematite phase can be easily reduced to metallic Fe, which is then rapidly carburized in the presence of CO. The reduction feature of hematite to magnetite (Fe_3O_4) shifted from 270 °C to 330 °C with increasing chromium content. The start of the reduction of magnetite was delayed from 280 °C for Cr(0) to 360 °C for Cr(12). Small reduction features between 150 °C and 230 °C relate to the reduction of a small amount of hexavalent chromium, which is most likely present at the surface in chromium-containing samples [38]. This reduction feature is indeed absent in the CO-TPR pattern of the chromium-free Cr (0) (Fig. 5). CO_2 evolution observed at ~500 °C, prevalent in all reduction patterns, can be attributed to the Boudouard reaction. These results show that chromium doping delays the formation and over-reduction of magnetite, which is considered the active phase in the WGS reaction.

3.2. Catalytic activity

Fig. 6 shows the CO conversion of the catalysts under industrially relevant HTS conditions. After activation and ageing for 24 h at 450 °C at 25 bar, the catalytic performance was compared at 360 °C, away from equilibrium conditions. Clearly, the activity increased with chromium content. The trend was similar after a second 24 h ageing step at 450 °C with slightly higher activities for all samples at 360 °C. The promoting effect of chromium on the CO conversion is usually attributed to a higher surface area [1,5], which is in line with the textural properties of the calcined catalyst precursors (Table 2). The catalysts exposed to industrially relevant conditions for 4 days at 2 bar show a similar increasing CO conversion with increasing chromium content after the first and second thermal ageing step. The higher activities observed for chromium-doped catalysts at both reaction pressures indicate that the structural stabilisation by chromium doping is independent of pressure.

3.3. Used catalyst

After the HTS reaction, the catalyst samples were stored and transported under argon to prevent oxidation of the active magnetite catalysts to maghemite. The used catalysts were investigated with XRD, Mössbauer spectroscopy, and XPS. Mössbauer parameters computed by DFT using various magnetite structural models were used to interpret the experimental Mössbauer spectra.

The XRD patterns of the used catalysts, after exposure to industrially relevant HTS conditions for 4 days at 25 and 2 bar, show reflections that can be attributed to either magnetite or maghemite (Fig. 7). The presence of maghemite is, however, unlikely during the reaction because it will typically convert into magnetite under WGS conditions [5]. These findings also show that the formation of magnetite does not depend on the reaction pressure.

Decreasing crystallite sizes were observed with increasing chromium content (Table 4), independent of the reaction pressure, which is in line with the proposal that chromium prevents sintering of the magnetite phase [1,2].

Before discussing the Mössbauer spectra of the used catalysts primarily consisting of magnetite, we first discuss the results of the

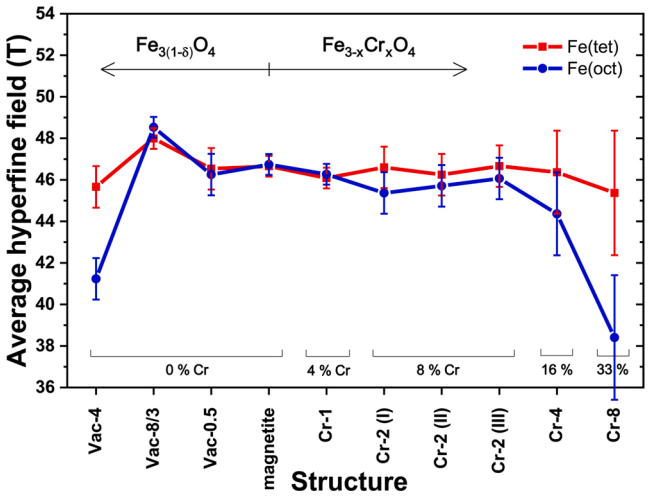

Fig. 8. Hyperfine magnetic field values for tetrahedral and octahedral Fe in various magnetite reference structures calculated by DFT. The Vac-8/3 structure represents maghemite.

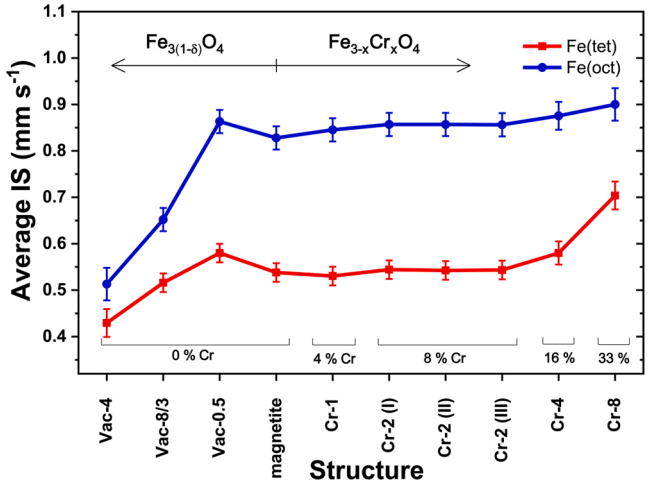

Fig. 9. IS values for tetrahedral and octahedral Fe of various magnetite reference structures determined by DFT calculations. The Vac-8/3 structure represents maghemite.

calculations of hyperfine parameters for different magnetite structures, *i.e.*, magnetite, magnetite with octahedral Fe vacancies ($Fe_{3(1-\delta)}O_4$), and chromium-doped magnetite ($Fe_{3-x}Cr_xO_4$) where Fe^{3+} in octahedral positions is replaced by Cr^{3+}.

The calculated hyperfine magnetic field values are displayed in Fig. 8, with error bars reflecting the dispersion of values in a given Fe sublattice and the estimated overall uncertainty due to the computational setup. Slightly higher octahedral and tetrahedral hyperfine magnetic field values are predicted for maghemite (Vac-8/3) in comparison to the non-doped magnetite structure. This is in line with experimental data for these two structures [34]. Vacancy doping has a negligible effect on the hyperfine magnetic field values when the vacancy content was low (Vac-0.5), whereas a significant decrease in the octahedral hyperfine magnetic field was observed for the $Fe_{3(1-\delta)}O_4$ structure with a higher vacancy content (Vac-4). It should be pointed out, however, that the Vac-4 structure will likely not occur in practice, because its vacancy content is higher than that of maghemite (Vac-8/3). Maghemite can be regarded as fully oxidized magnetite. Therefore, it can be concluded that the influence of vacancy doping on the hyperfine magnetic field values is small. On the other hand, the octahedral hyperfine magnetic field value decreases with increasing substitution of octahedral Fe by Cr. This

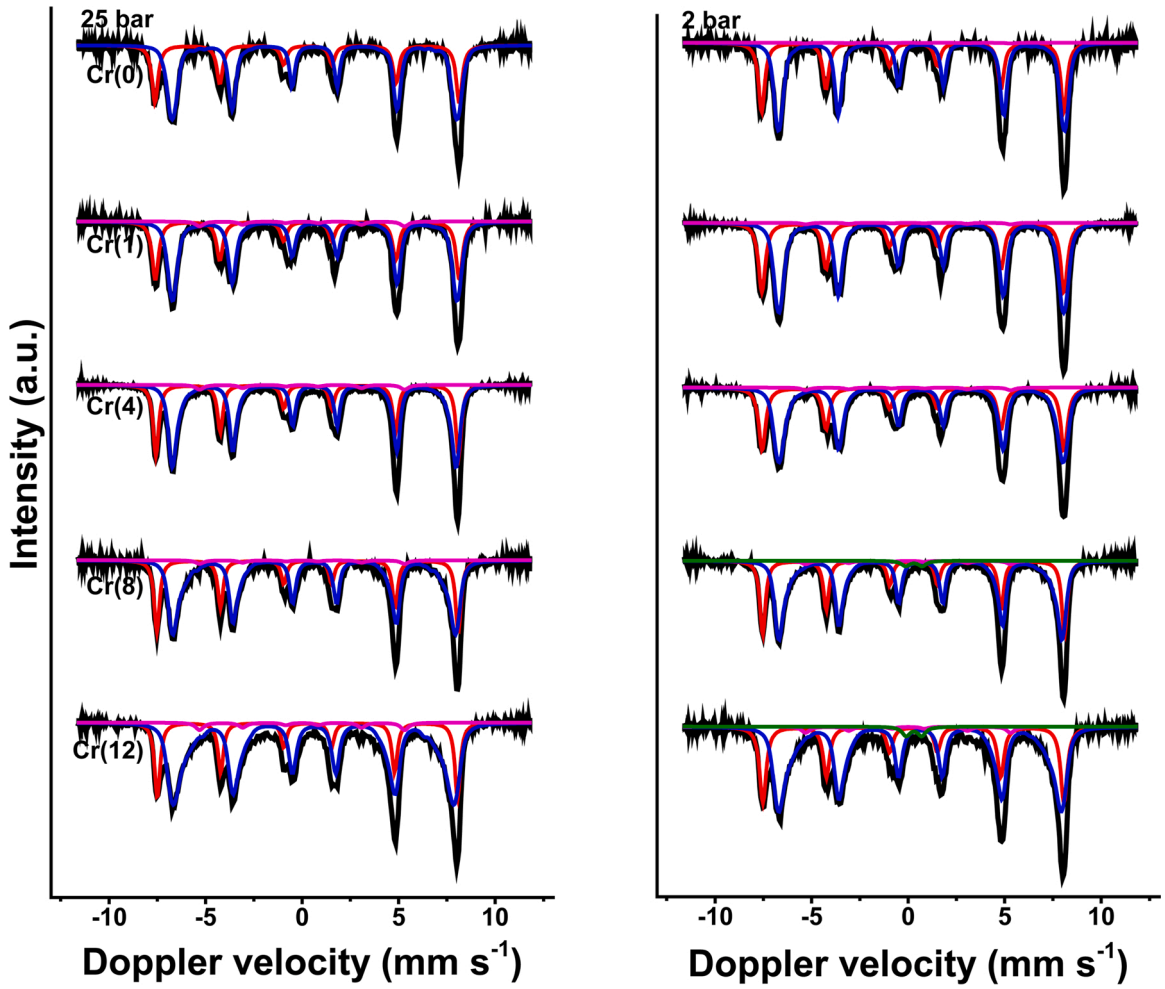

Fig. 10. Mössbauer spectra of used catalysts at 25 bar (left) and 2 bar (right).

substitution in octahedral sites did not affect the tetrahedral hyperfine magnetic field values as much.

The IS values computed for the tetrahedral and octahedral Fe sites in reference structures are shown in Fig. 9. The IS values of the octahedral sites are typically higher than those of the tetrahedral sites. The higher octahedral IS values can be explained by the presence of both Fe^{3+} and Fe^{2+} in these sites, whereas the tetrahedral sites are only occupied by Fe^{3+}. For the vacancy-doped Vac-8/3 and Vac-4 structures, a significant decrease of the octahedral IS values is predicted, which demonstrates that the absence of Fe^{2+} results in a lower IS compared to the mixed-valence (Fe^{3+}/Fe^{2+}) octahedral sites in stoichiometric magnetite. Introducing chromium results in higher octahedral IS values in the $Fe_{3-x}Cr_xO_4$ structures. The higher IS values can be explained by the replacement of octahedral Fe^{3+} by Cr^{3+}, resulting in a lower Fe^{3+}/Fe^{2+} ratio of the octahedral B sites. The computed tetrahedral IS values for the Cr-4 and Cr-8 structures are higher than those of the Cr-1 and Cr-2 structures. This trend is in line with the high IS value observed for chromite ($FeCr_2O_4$) where the tetrahedral sites are completely occupied by Fe^{2+} ions [39].

In summary, modelling shows that incorporation of chromium in octahedral sites results in a decrease of the hyperfine magnetic field for the octahedral Fe sites, whereas the hyperfine magnetic field of tetrahedral Fe remains unaffected. The influence of octahedral vacancies on the hyperfine magnetic field is negligible. The data also show a significant effect of chromium doping on octahedral IS values due to a change in the Fe^{3+}/Fe^{2+} ratio. The following trends can be discerned: when Fe^{3+} is replaced by Cr^{3+}, the octahedral IS value increases with Cr

Table 5
Catalysts after exposure to HTS conditions for 4 days at 25 bar.

Sample	Phase	IS (mm s^{-1})	QS (mm s^{-1})	H (T)	Γ (mm s^{-1})	Spectral contribution (%)
Cr(0)	Fe_3O_4(tet)	0.26	−0.03	48.7	0.38	38
	Fe_3O_4(oct)	0.68	−0.03	45.7†[a]	0.32	62
	α-Fe	0.00*	0.00*	33.0*[a]	0.50*	1
Cr(1)	Fe_3O_4(tet)	0.27	−0.03	48.6	0.43	37
	Fe_3O_4(oct)	0.67	0.03	45.6†	0.37	62
	α-Fe	0.00*	0.00*	33.0*	0.50*	1
Cr(4)	Fe_3O_4(tet)	0.27	−0.02	48.6	0.43	37
	Fe_3O_4(oct)	0.66	0.01	45.3†	0.38	62
	α-Fe	0.00*	0.00*	33.0*	0.50*	2
Cr(8)	Fe_3O_4(tet)	0.28	0.00	48.6	0.34	34
	Fe_3O_4(oct)	0.64	−0.01	44.6†	0.32	61
	α-Fe	0.00*	0.00*	33.0*	0.50*	2
	SPM	0.30*	0.86	–	0.50*	2
Cr(12)	Fe_3O_4(tet)	0.28	−0.01	48.4	0.41	31
	Fe_3O_4(oct)	0.63	−0.02	44.1†	0.40	64
	α-Fe	0.00*	0.00*	33.0*	0.50*	3
	SPM	0.30*	0.80*	–	0.50*	2

[a]Fixed values are marked with an asterisk (*), average values with a dagger (†).
[b]Experimental uncertainties: IS ± 0.01 mm s^{-1}, QS ± 0.01 mm s^{-1}, line width: Γ ± 0.01 mm s^{-1}, hyperfine magnetic field: ± 0.1 T, spectral contribution: ± 3%.
[c]Small amounts of α-Fe were observed in all catalysts with no clear correlation to Cr content. The small SPM fraction present in some of the catalysts represents small particle magnetite.

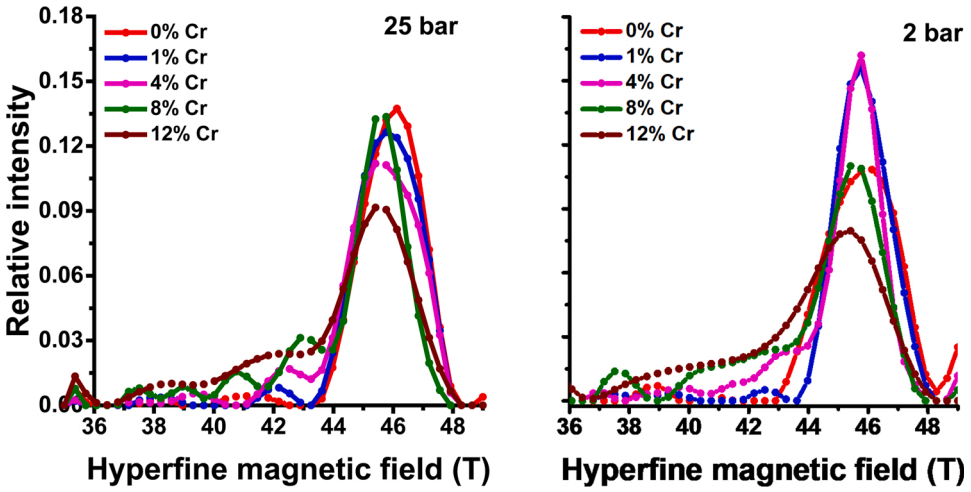

Fig. 11. Hyperfine magnetic field distributions of the octahedral sites of magnetite fitted for Mössbauer spectra in Fig. 10, 25 bar (left), 2 bar (right).

Table 6
Hyperfine parameters determined by fitting Mössbauer spectra of used catalysts after exposure to HTS conditions for 4 days at 2 bar.

Sample	Phase	IS (mm s^{-1})	QS (mm s^{-1})	H (T)	Γ (mm s^{-1})	Spectral contribution (%)
Cr(0)	Fe_3O_4(tet)	0.28	−0.04	49.0	0.38	35
	Fe_3O_4(oct)	0.64	−0.00	45.6†	0.29	63
	α-Fe	0.00*	0.00*	33.0*	0.50*	2
Cr(1)	Fe_3O_4(tet)	0.28	−0.03	48.9	0.41	35
	Fe_3O_4(oct)	0.65	0.01	45.6†	0.39	62
	α-Fe	0.00*	0.00*	33.0*	0.50*	4
Cr(4)	Fe_3O_4(tet)	0.28	−0.03	48.7	0.34	35
	Fe_3O_4(oct)	0.65	−0.03	45.1†	0.32	61
	α-Fe	0.00*	0.00*	33.0*	0.50*	4
Cr(8)	Fe_3O_4(tet)	0.29	−0.01	48.5	0.33	33
	Fe_3O_4(oct)	0.64	−0.02	44.3†	0.33	65
	α-Fe	0.00*	0.00*	33.0*	0.50*	3
Cr(12)	Fe_3O_4(tet)	0.28	−0.01	48.3	0.34	27
	Fe_3O_4(oct)	0.61	−0.03	43.6†	0.41	70
	α-Fe	0.00*	0.00*	33.0*	0.50*	4

[a]Fixed values are marked with an asterisk (*), average values with a dagger (†).
[b]Experimental uncertainties: IS ± 0.01 mm s^{-1}, QS ± 0.01 mm s^{-1}, line width: Γ ± 0.01 mm s^{-1}, hyperfine magnetic field: ± 0.1 T, spectral contribution: ± 3%.
[c]Small amounts of α-Fe were observed in all catalysts with no clear correlation with the Cr content.

content. In structures where Cr^{3+} replaces an equal amount of Fe^{3+} and Fe^{2+} in the octahedral sites, the octahedral isomer shift is unaffected by chromium doping. In a structure where the presence of octahedral Cr^{3+} prevents the reduction of Fe^{3+} to Fe^{2+}, the octahedral IS will decrease with increased chromium content.

The computed hyperfine parameters will be used to discuss the experimentally obtained parameters with a focus on the impact of chromium incorporation. Room-temperature Mössbauer spectra of used catalysts after treatment for 4 days at 2 and 25 bar are shown in Fig. 10. These spectra were fitted with two sub-spectra representing Fe^{3+} in tetrahedral sites and mixed valence Fe^{2+}/Fe^{3+} in octahedral sites. A decreasing trend in the hyperfine magnetic field values of the octahedral sites from 45.7 T to 44.1 T was observed with increasing chromium content for the used catalysts after treatment at 25 bar (Table 5). The hyperfine magnetic field values of the tetrahedral sites did not vary significantly (48.6 T +/- 0.1 T) for the used Cr(0)–Cr(8) catalysts with a slightly lower value of 48.4 T being observed for the used Cr(12) catalyst. A decrease in the hyperfine magnetic field can be the result of chromium incorporation or smaller crystallites [36]. The finding that the hyperfine magnetic fields of the tetrahedral sites did not change much with chromium content shows that a particle size effect is unlikely. Together with the modelling results, it can be concluded that chromium is incorporated in the octahedral sites of magnetite. The octahedral components were fitted with a hyperfine magnetic field distribution (Fig. 11). The hyperfine magnetic field distribution was

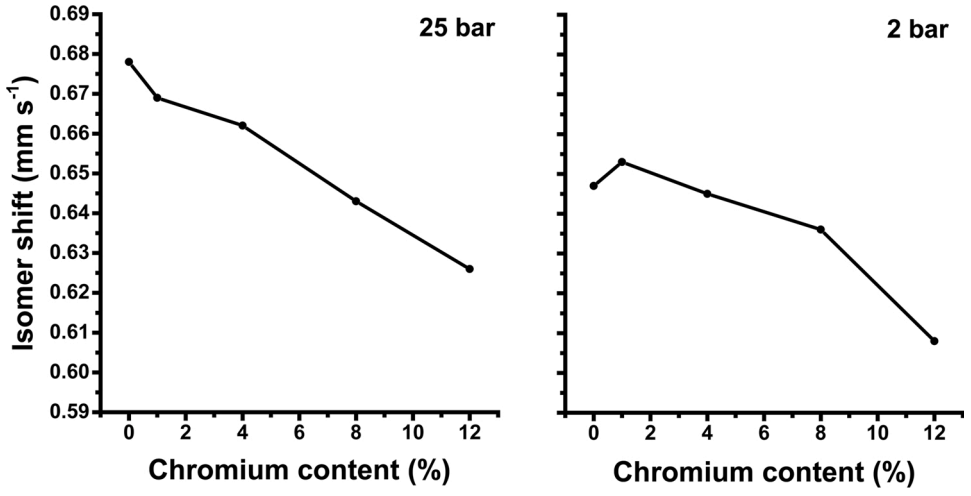

Fig. 12. IS values of the octahedral sites of magnetite compared to chromium doping fitted for Mössbauer spectra in Fig. 10, 25 bar (left), 2 bar (right).

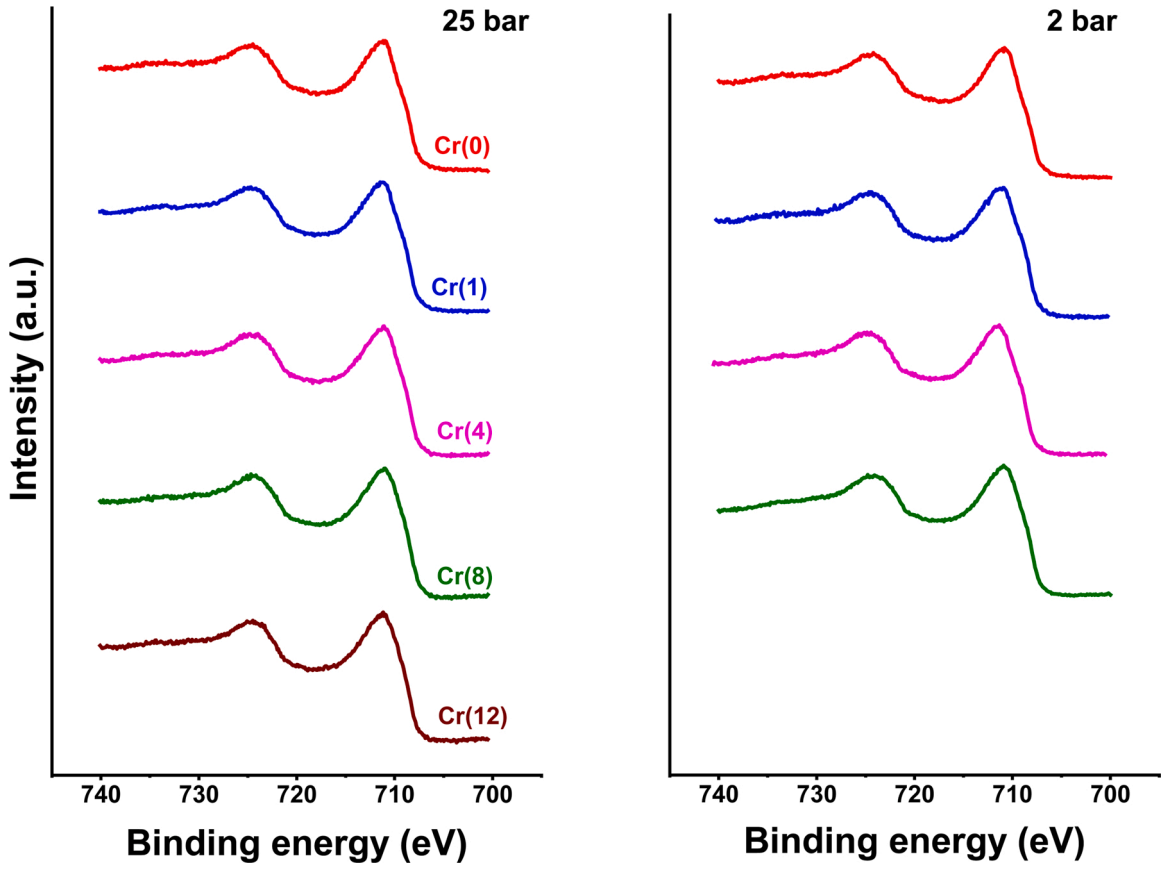

Fig. 13. Fe 2p region of used catalysts after treatment for 4 days at 25 bar (left) and 2 bar (right).

seen to broaden as the chromium content increases. This trend confirms that chromium is incorporated into octahedral sites of the active magnetite phase in HTS catalysts [36].

The octahedral IS values decreased with increasing chromium content in the used catalysts after treatment at 25 bar (Table 6, Fig. 12). The IS value, which is 0.68 mm s^{-1} for the non-doped Cr(0) sample, decreases with increasing chromium content to 0.63 mm s^{-1} for the Cr(12) sample. The IS provides information about the oxidation state of Fe [40]. The bulk IS value of the octahedral sites of magnetite of ~0.67 mm s^{-1} at room temperature is the average of fast electron hopping between Fe^{2+} and Fe^{3+} ions in octahedral sites [41]. As this electron hopping is faster than the lifetime of an excited nuclear state in the Mössbauer experiment, the bulk IS value of ~0.67 mm s^{-1} represents an average 2.5+ state of the Fe ions in octahedral sites [41]. IS values of ~0.3 mm s^{-1} are common for Fe^{3+}-oxide species. Thus, the lower IS value observed upon chromium doping indicates a higher than unity Fe^{3+}/Fe^{2+} ratio in the octahedral sites [42,43].

Mössbauer spectra of catalysts treated for 4 days at 2 bar also show the presence of a magnetite phase (Fig. 10). A similar decreasing trend in IS values with chromium content (Fig. 12) was observed, indicating that chromium results in a higher Fe^{3+}/Fe^{2+} ratio in octahedral sites of magnetite also at a relatively low reaction pressure. Although Fig. 12 may suggest that the octahedral sites of catalysts treated at 2 bar contain a higher Fe^{3+}/Fe^{2+} ratio than those treated at 25 bar, the differences are within the accuracy of the IS measurement (+/-0.01 mm s^{-1}). The broadening hyperfine magnetic field distributions of the octahedral sites evident from Fig. 11 confirm the incorporation of chromium into the structure. Different from the 25 bar results, a decrease of the hyperfine magnetic fields of the tetrahedral sites with increasing chromium content can be observed. This decrease is however much smaller (0.7 T) compared to the decrease in hyperfine magnetic fields of octahedral sites (2.0 T). As discussed before, this difference indicates that particle sizes effects can most likely be excluded. An alternative explanation for the high tetrahedral hyperfine magnetic fields in the Cr(0) and Cr(1) samples is that some accidental oxidation occurred to maghemite, which typically has a hyperfine magnetic field of ~50 T [34]. Partially oxidized magnetite can explain the IS value of the Cr(0) sample below the bulk value of 0.67 mm s^{-1} (Table 6).

The modelled hyperfine parameters combined with the experimental data allow us to revisit the chromium incorporation models discussed in the introduction. Zhu and Wachs [1] conclude in their recent review on HTS catalysts that Cr^{3+} replaces octahedral Fe^{3+} in structure 1 (see below). Robbins et al. [14] suggested that Cr replaces an equal amount of octahedral Fe^{2+} and Fe^{3+}, which after charge compensation leads to structure 2. Rangel et al. [17] proposed that the octahedral site preference of Cr^{3+} prevents Fe^{3+} reduction during formation of the active phase. This structure is best represented as structure 3. Based on the calculated hyperfine parameters discussed above, it can be concluded that the incorporation of chromium in octahedral positions, suggested in all models, will decrease the octahedral hyperfine magnetic field. The decreasing octahedral hyperfine magnetic field confirmed the incorporation of chromium into octahedral sites in our catalysts obtained after the HTS reaction at 2 and 25 bar. For structure 1, the computed octahedral IS values predict an increasing trend with Cr doping. In contrast, these octahedral IS value should remain unaffected for structure 2. The experimentally observed decreasing trend in octahedral IS values shows that these models do not accurately describe the cation distribution in the octahedral sites for our catalysts. Instead, the decreasing experimental octahedral IS values show that chromium incorporation in the octahedral sites results in an increased Fe^{3+}/Fe^{2+} ratio as is the case in structure 3. Since the tetrahedral sites are unaffected by Cr incorporation, structure 3 can be simplified as $Fe_{3-x(1-\delta)}Cr_xO_4$, where x describes the octahedral Cr content and δ the octahedral Fe vacancy content. Thus, chromium incorporation prevents Fe^{2+} formation during magnetite

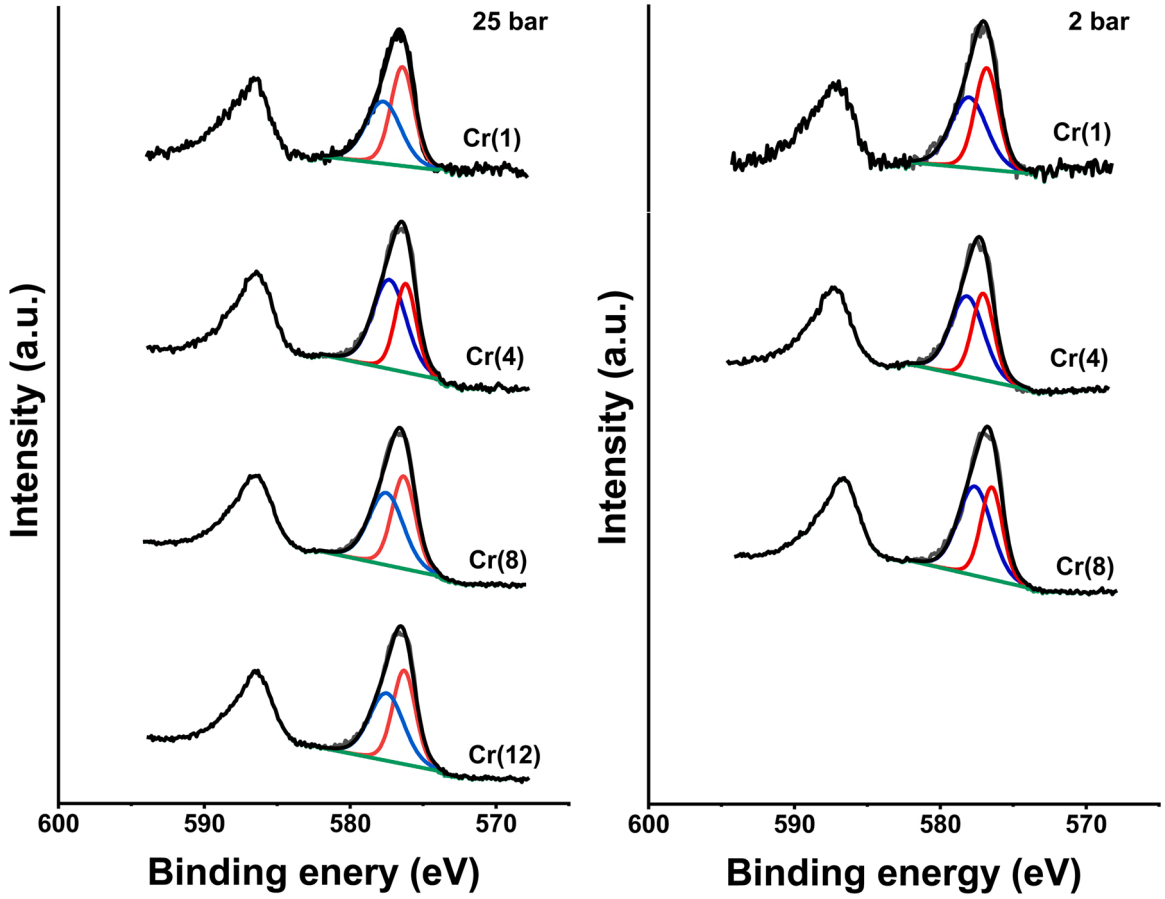

Fig. 14. Cr 2p region of used catalysts after treatment for 4 days at 25 bar (left) and 2 bar (right).

formation. The presence of such a $Fe_{3-x(1-\delta)}Cr_xO_4$ structure has not been demonstrated before in *in situ* formed HTS catalysts. The resulting partially oxidized chromium-doped magnetite structure had no negative effect on the high CO conversion typically associated with chromium doping.

$$(Fe_1^{3+})\left[Fe_{1-x}^{3+}Cr_x^{3+}Fe_1^{2+}\right]O_4 \quad (1)$$

$$(Fe_1^{3+}+Fe_x^{2+})\left[Fe_{1-x}^{3+}Cr_{2x}^{3+}Fe_{1-x}^{2+}\right]O_4 \quad (2)$$

$$(Fe_1^{3+})\left[Fe_{1-x}^{3+}Cr_x^{3+}Fe_{1-y}^{2+}+\delta\right]O_4 \quad (3)$$

The surface of the used catalysts was investigated by XPS analysis. The Fe 2p region of the catalysts after exposure to HTS conditions for 4 days at 2 and 25 bar is shown in Fig. 13. The Fe $2p_{3/2}$ peak of Fe^{3+}-oxide containing hematite is typically found at a BE between 710.6 and 711.2 eV, while the Fe $2p_{3/2}$ peak of Wüstite Fe^{2+}-oxide appears at a slightly lower BE of 709.5 eV. The Fe $2p_{3/2}$ peak for the mixed valence Fe^{3+}/Fe^{2+}-oxide containing magnetite usually appears between these values at BE =710.6 eV [44]. This makes identification of these Fe-oxides difficult from spectral fitting alone. Pure Fe^{3+}-phases like hematite can also be identified from the satellite peak in the Fe 2p region at BE =719 eV, while Fe^{2+}-phases like Wüstite are characterized by a satellite peak at BE =715.5 eV. A unique property of the Fe 2p region of magnetite is the absence of these Fe^{3+} and Fe^{2+} satellite peaks. The absence of satellite features at BE =719 eV and 715.5 eV indicates that the surface is dominated by magnetite [44]. This implies that there are no structural differences between the surface and the bulk.

The XPS spectra of the Cr 2p region are shown in Fig. 14. Spectral fitting following a procedure from literature [5] revealed the presence of Cr^{3+} species with the Cr $2p_{3/2}$ peak at BE = 576.5−577 eV. A simple fitting model was chosen to prevent over-interpretation of the complex Cr 2p region. The absence of a sharp peak at BE = ~580 eV indicates that no Cr^{6+} is present on the catalysts surface after 4 days on stream, indicating the complete conversion of Cr^{6+} in the catalyst precursor to Cr^{3+} species. Chromium is present as Cr^{3+} in the activated catalysts.

4. Conclusions

HTS catalysts prepared *via* co-precipitation and calcination consist of hematite in which chromium can be doped (α-$Fe_{2-x}Cr_xO_3$). Magnetite formation and over-reduction of the active magnetite phase to α-Fe occur at higher temperatures in chromium-containing samples. Chromium-doped magnetite was formed after exposure of the calcined samples to industrially relevant HTS conditions. The presence of chromium led to higher activity, irrespective of the reaction pressure (2 or 25 bar). Chromium doping led to smaller crystallite sizes, confirming its role as a structural promoter. Mössbauer evidenced the incorporation of chromium in octahedral sites of magnetite, preventing reduction of Fe^{3+} ions during magnetite formation and leading to an increased Fe^{3+}/Fe^{2+} ratio in octahedral sites. Interpretation of Mössbauer spectra was supported by DFT calculation of hyperfine parameters of various chromium and Fe-vacancy doped magnetite structures. The variations in the Fe^{3+}/Fe^{2+} ratio due to Cr doping had no measurable effect on the CO conversion levels associated with Cr-doping. The structural characterization shows that the active phase under industrial HTS conditions is best described by $Fe_{3-x(1-\delta)}Cr_xO_4$ structure, in which Cr^{3+} is doped in the octahedral sites and its presence during the formation of the active phase prevents Fe^{2+} formation, resulting in a partially oxidized structure compared to stoichiometric magnetite.

CRediT authorship contribution statement

M.I. Ariens: Methodology, Investigation, Data curation, Formal analysis, Validation, Writing – original draft, **V. Chlan**: Software, Modeling, Formal Analysis. **P. Novak**: Software, Modeling, Formal Analysis. **L.G.A. van de Water**: Conceptualization, Methodology, Writing – review & editing, Supervision. **A.I. Dugulan**: Methodology, Investigation, Formal analysis, Validation, Writing – review & editing, Supervision. **E. Brück**: Conceptualization, Writing – review & editing, Supervision, Project administration. **E.J.M. Hensen**: Conceptualization, Writing – review & editing, Supervision, Project administration.

Declaration of Competing Interest

The authors report no declarations of interest.

Acknowledgements

This publication is part of the project Application of advanced combined in-situ Mössbauer/IR/GC characterisation under industrially relevant conditions to underpin and accelerate development of improved Fe-based catalysts with project number 731.015.419 of the research programme LIFT, which is (partly) financed by the Dutch Research Council (NWO). The authors would like to thank Arno van Hoof for the TEM measurements and Freddy Oropeza for his assistance and advice on the XPS measurements. Deborah Dodds for her advice and training in catalyst preparation and Michel Steenvoorden for his help with the Mössbauer spectroscopy setup.

References

[1] Minghui Zhu, E.Wachs Israel, Iron-based catalysts for the high-temperature water-gas shift (HT-WGS) reaction: a review, ACS Catal. 6 (2016) 722–732.
[2] Dae-Won Lee, Myung Suk Lee, Joon Yeob Lee, Seongmin Kim, Hee-Jun Eom, Dong Ju Moon, Kwan-Young Lee, The review of Cr-free Fe-based catalysts for high-temperature water-gas shift reactions, Catal. Today 210 (2013) 2–9.
[3] S. David, Newsome the water-gas shift reaction, Catal. Rev. Sci. Eng. 21 (1980) 275–318.
[4] Martyn V. Twigg, Catalyst Handbook, 2 ed., 1989.
[5] Christopher J. Keturakis, Minghui Zhu, Emma K. Gibson, Marco Daturi, Franklin Tao, Anatoly I. Frenkel, Israel E. Wachs, Dynamics of CrO_3-Fe_2O_3 catalysts during the high-temperature water-gas shift reaction: molecular structures and reactivity, ACS Catal. 6 (2016) 4786–4798.
[6] Devaiah Damma, Panagiotis G. Smirniotis, Recent advances in iron-based high-temperature water-gas shift catalysis for hydrogen production, Curr. Opin. Chem. Eng. 21 (2018) 103–110.
[7] Ataullah Khan, Panagiotis G. Smirniotis, Relationship between temperature-programmed reduction profile and activity of modified ferrite-based catalysts for WGS reaction, J. Mol. Catal. A Chem. 280 (2008) 43–51.
[8] Gareth S. Parkinson, Iron oxide surfaces, Surf. Sci. Rep. 71 (2016) 272–365.
[9] J.E. Kubsh, J.A. Dumesic, In situ gravimetric studies of the regenerative mechanism for water-gas shift over magnetite: equilibrium and kinetic measurements in CO_2/CO and H_2O/H_2 gas mixtures. American Institute of Chemical Engineers 28 (1982) 793–800.
[10] G.K. Boreskov, T.M. Yurieva, A.S. Sergeeva, Mechanism of the conversion of carbon monoxide on iron-chromium catalyst, React. Kinet. Catal. Lett. 11 (1970) 374–381.
[11] Gunugunuri K. Reddy, Seok Jhin Kim, Junhang Dong, Panagiotis G. Smirniotis, Jacek B. Jasinski, Long-term WGS stability of Fe/Ce and Fe/Ce/Cr catalysts at high and low steam to CO ratios—XPS and Mössbauer spectroscopic study, Appl. Catal. A Gen. 415-416 (2012) 101–110.
[12] Sittichai Natesakhawat, Xueqin Wang, Lingzhi Zhang, Umit S. Ozkan, Development of chromium-free iron-based catalysts for high-temperature water-gas shift reaction, J. Mol. Catal. A Chem. 260 (2006) 82–94.
[13] Minghui Zhu, Israel E. Wachs, A perspective on chromium-Free iron oxide-based catalysts for high temperature water-gas shift reaction, Catal. Today 311 (2018) 2–7.
[14] M. Robbins, G.K. Wertheim, R.C. Sherwood, D.N.E. Buchanan, Magnetic properties and site distributions in the system $FeCr_2O_4$-Fe_3O_4($Fe^{2+}Cr_{2-x}Fe^{3+}{}_xO_4$), J. Phys. Chem. Solids 32 (1971) 717–729.
[15] H. Topsøe, M. Boudart, Mössbauer spectroscopy of CO shift catalysts promoted with lead, J. Catal. 31 (1973) 346–359.
[16] Gunugunuri K. Reddy, P. Boolchand, Panagiotis G. Smirniotis, Sulfur tolerant metal doped Fe/Ce catalysts for high temperature WGS reaction at low steam to CO ratios – XPS and Mössbauer spectroscopic study, J. Catal. 282 (2011) 258–269.
[17] Mariado Carmo Rangel, Renato Massami Sassaki, Fernando Galembeck, Effect of chromium on magnetite formation, Catal. Letters 33 (1995) 237–254.
[18] Minghui Zhu, Tulio C.R. Rocha, Thomas Lunkenbein, Axel Knop-Gericke, Robert Schlögl, Israel E. Wachs, Promotion mechanisms of iron oxide-based high temperature water-gas shift catalysts by chromium and copper, ACS Catal. 6 (2016) 4455–4464.
[19] Minghui Zhu, Pengfei Tian, Ravi Kurtz, Thomas Lunkenbein, Jing Xu, Robert Schlögl, Israel E. Wachs, Yi-Fan Han, Strong metal–support interactions between copper and iron oxide during the high-temperature water-gas shift reaction, Angew. Chemie 131 (2019) 9181–9185.
[20] Minghui Zhu, Pengfei Tian, Jiacheng Chen, Michael E. Ford, Xu Jing, Israel E. Wachs, Yi-Fan Han, Activation and deactivation of the commercial-type CuO-Cr_2O_3-Fe_2O_3 high temperature shift catalyst, Am. Inst. Chem. Eng. 66 (2019) 1–6.
[21] C. Pellerin, S.M. Booker, Reflections on hexavalent chromium: health hazards of an industrial heavyweight, Environ. Health Perspect. 108 (2000) 402–407.
[22] Rudolf L. Mössbauer, Kernresonanzfluoreszenz von Gammastrahlung in Ir^{191}, Zeitschrift fur Physik 151 (1958) 124–143.
[23] Jingxiu Xie, Hirsa M.Torres Galvis, Ard C.J. Koeken, Alexey Kirilin, A. Iulian Dugulan, Matthijs Ruitenbeek, Krijn P. de Jong, Size and promoter effects on stability of carbon-nanofiber-supported iron-based Fischer-Tropsch catalysts, ACS Catal. 6 (2016) 4017–4024.
[24] Vera P. Santos, Tim A. Wezendonk, Juan José Delgado Jaén, A. Iulian Dugulan, Maxim A. Nasalevich, Husn-Ubayda Islam, Adam Chojecki, Sina Sartipi, Xiaohui Sun, Abrar A. Hakeem, Ard C.J. Koeken, Matthijs Ruitenbeek, Thomas Davidian, Garry R. Meima, Gopinathan Sankar, Freek Kapteijn, Michiel Makkee, Jorge Gascon, Metal organic framework-mediated synthesis of highly active and stable Fischer-Tropsch catalysts, Nat. Commun. 6 (2015) 6451.
[25] Ř. Reznícek, V. Chlan, H. Štěpánková, P. Novák, Hyperfine field and electronic structure of magnetite below the Verwey transition, Phys. Rev. B 15 (2015) 125–134.
[26] Fereshteh Meshkani, Mehran Rezaei, Preparation of mesoporous chromium promoted magnetite based catalysts for high temperature water gas shift reaction, Ind. Eng. Chem. Res. 45 (2015) 1236–1242.
[27] A.A. Moolenaar, PhD Thesis, Delft University of Technology, 1994. ISBN 90-73861-20-29.
[28] Zoltán Klencsár, Mössbauer spectrum analysis by evolution algorithm, Nucl. Instrum. Methods Phys. Res. B 129 (1997) 527–533.
[29] P. Blaha, K. Schwarz, G.K.H. Madsen, D. Kvasnicka, J. Luitz, Wien2K, Technische Universitat Wien, 2001.
[30] R. Reznícek, V. Chlan, H. Štepánková, P. Novák, J. Zukrowski, A. Kozlowski, Z. Kakol, Z. Tarnawski, J.M. Honig, Understanding the Mössbauer spectrum of magnetite below the Verwey transition: *ab initio* calculations, simulation, and experiment, Phys. Rev. B 96 (2017), 195124.
[31] P. Novák, V. Chlan, Contact hyperfine field at Fe nuclei from density functional calculations, Phys. Rev. B 81 (2010), 174412.
[32] Minghui Zhu, Özgen Yalçin, Israel E. Wachs, Revealing structure-activity relationships in chromium free high temperature shift catalysts promoted by earth abundant elements, Appl. Catal. B 232 (2018) 205–212.
[33] Tiberiu Popa, Xu Guoqing, Thomas F. Barton, Morris D. Argyle, High temperature water gas shift catalysts with alumina, Appl. Catal. A Gen. 379 (2010) 15–23.
[34] R.M. Cornel, U. Schwertmann, The Iron Oxides: Structures, Properties, Reactions, Occurences and Uses, 2003, pp. 155–156.
[35] Özden Özdemir, David J. Dunlop, Thelma S. Berquó, Morin transition in hematite: size dependence and thermalhysteresis, Geochem. Geophys. Geosystems 9 (2008) 1–12.
[36] Enver Murad, John Cashion, Mössbauer Spectroscopy of Environmental Materials and Their Industrial Utilization, 2004.
[37] G. Doppler, A.X. Trautwein, H.M. Ziethen, Physical and catalytic properties of high-temperature water-gas shift catalysts based upon iron-chromium oxides, Appl. Catal. 40 (1988) 119–130.
[38] Gunugunuri K. Reddy, Kapila Gunasekara, P. Boolchand, Panagiotis G. Smirniotis, Cr- and Ce-doped ferrite catalysts for the high temperature water-gas shift reaction: TPR and mössbauer spectroscopic study, J. Phys. Chem. C 115 (2011) 920–930.
[39] Shin Nakamura, Akio Fuwa, Spin order in $FeCr_2O_4$ observed by Mössbauer spectroscopy, Phys. Procedia 75 (2015) 747–754.
[40] Francis Menil, Systematic trends of the ^{57}Fe Mössbauer isomer shifts in (FeO_n) and (FeF_n) polyhedra. Evidence of a new correlation between the isomer shift and the inductive effect of the competing bond T-X (-> Fe) (where X is O or F and T any element with a formal positive charge), J. Phys. Chem. Solids 46 (1984) 763–789.
[41] Christopher A. Gorski, Michelle M. Scherer, Influence of magnetite stoichiometry on Fe^{II} uptake and nitrobenzene reduction, Environ. Sci. Technol. 43 (2009) 3675–3680.
[42] Zoltán Klencsár, Attila Ábrahám, L.ászló Szabó, Ervin Gy Szabó, S.á ndor Stichleutner, Ernő Kuzmann, Zoltán Homonnay, Gyula Tolnai, The effect of preparation conditions on magnetite nanoparticles obtained via chemical co-precipitation, Mater. Chem. Phys. 223 (2019) 122–132.
[43] C.E. Johnson, J.A. Johnson, H.Y. Hah, M. Cole, S. Gray, V. Kolesnichenko, P. Kucheryavy, G. Goloverda, Mössbauer studies of stoichiometry of Fe_3O_4: characterization of nanoparticles for biomedical applications, Hyperfine Interact. 237 (2016) 27-1–27-10.
[44] Toru Yamashita, Peter Hayes, Analysis of XPS spectra of Fe^{2+} and Fe^{3+} ions in oxide materials, Appl. Surf. Sci. 254 (2008) 2441–2449.